Aggregate defects of gold and platinum with lithium in silicon: II. Electronic-structure calculations

H. Weihrich, H. Overhof, P. Alteheld, S. Greulich-Weber, and J.-M Spaeth
Fachbereich Physik, Universität-Gesamthochschule Paderborn, D-33095 Paderborn, Federal Republic of Germany
(Received 17 January 1995)

We present *ab initio* total energy calculations for aggregate defects of the noble metals Pt or Au with Li. The calculations are performed in the local spin density approximation to the density-functional theory using the linear-muffin-tin-orbital method in the atomic spheres approximation. We determine the binding energies of the aggregates (ignoring lattice relaxations) and calculate the hyperfine interactions. We show that in the aggregate defects observed experimentally (see paper I) the noble metal atom is always on a lattice site. There is a stable orthorhombic pair consisting of one Li atom on an interstitial site close to the noble metal impurity and a trigonal aggregate consisting of the noble metal surrounded by three Li atoms on the nearest interstitial sites. The hyperfine interactions (see paper I) with the noble metal, with Li, and also with Si are quantitatively explained by an extension of the vacancy model and it is shown that the ^{29}Si nucleus giving rise to the prominent hyperfine interaction is on a regular lattice site. We show that aggregates involving two Li atoms are not stable. There is, however, a stable aggregate where four Li atoms are placed around one Pt atom in a tetrahedral configuration. The analogous aggregate with Au has no state in the gap and, therefore, would be a stable end product of the gettering process of Au by Li. Its presence might be difficult to prove experimentally.

I. INTRODUCTION

With electron paramagnetic resonance (EPR) and electron nuclear double resonance (ENDOR), the symmetry of aggregate defects of the noble metals Au and Pt with Li has been determined (see the preceding paper,[1] in the following to be referred to as part I). We, thus, know that within experimental accuracy, the defects have orthorhombic or trigonal symmetry, respectively. The orthorhombic defects consist of one noble metal atom and one Li atom on a cubic axis. For the trigonal aggregates, the experiments show that the noble metal and one Si atom are on the trigonal axis, while three Li atoms are placed on three equivalent mirror planes.

In order to establish a microscopic model of the aggregate defects, one has to know which of the atoms are built in on substitutional lattice sites, which are interstitials, and what the interatomic distances are. This information cannot be obtained from the experimental data. From the order of magnitude agreement of the observed hyperfine interactions (hfi) with the Pt nucleus for our aggregate defects with that observed for isolated Pt (which is identified as substitutional Pt_{Si}^{-} with an orthorhombic lattice distortion of the nearest neighbor ligands,[2]) one is led to assume substitutional noble metal atoms in the aggregate defects as well. All aggregate defects show hfi with one shell of Si nuclei, which exceeds the hfi with the other Si nuclei by one order of magnitude. From the experimental data one has no indication as to whether the Si atom is on a regular lattice site or on an interstitial position.

In this paper, we show that theoretical total energy calculations provide a powerful tool for the development of an atomic model for the aggregate defects: In Sec. II, we sketch the computational method, in Sec. III, we present the total energy results for isolated point defects and compare these with total energies calculated for different models for the aggregate defects. From a comparison of the total energies, we can decide whether a certain configuration is stable with respect to dissociation, whether it has a paramagnetic state, and what the ionization energy is of this state. Combining total energy results with spin densities obtained theoretically in comparison with hfi data obtained experimentally, one can discriminate whether a given model is a proper candidate for one of the aggregates found experimentally. In this way, we show that aggregates of the interstitial noble metals, Pt_i, or Au_i, with Li are not stable and that the calculated hfi data for these hypothetical aggregates are incompatible with the data presented in part I. In the same way, we show that the incorporation of Si self-interstitials Si_i into aggregate defects leads to a prominent hfi with a ^{29}Si nucleus that has not been observed experimentally. In Sec. III, we concentrate on defects where the noble metal atoms are substitutionally bound on regular lattice sites. We find stable aggregates of the noble metal ions: an orthorhombic pair defect with one Li and a trigonal aggregate involving three Li ions, which can be identified with the aggregates found experimentally in part I. In Sec. IV, we extend the vacancy model calculation of Anderson *et al.*[3,4] for isolated Pt point defects to these defect models. We show that our aggregate models explain quantitatively the measured hfi data of part I.

0163-1829/95/52(7)/5007(14)/$06.00

II. COMPUTATIONAL

The *ab initio* self-consistent electronic-structure calculations are performed using a Green function approach. In this approach, the problem separates into two parts, the calculation of the Green function G_0 for the perfect Si crystal, and the solution of a Dyson equation for Green function G of the crystal with the impurities. The Green function G_0 is calculated self-consistently treating exchange and correlation in the local spin-density approximation (LSDA) of the spin-density functional theory (DFT).[5,6] The Green function G for the infinite crystal with the impurities is obtained by a solution of Dyson's equation,

$$G = G_0 + G_0 \, \Delta V \, G \, . \tag{1}$$

Here, ΔV is the potential of the perturbation due to the impurities. Dyson's equation is solved self-consistently again using the DFT-LSDA method for an approximate treatment of the many-body effects.

In order to obtain theoretically the paramagnetic properties, we used a computational method that fairly represents wave functions in the vicinity of the nuclei. In this study, we used the linear-muffin-tin-orbital method in the atomic spheres approximation[7] (LMTO-ASA). In the LMTO-ASA method, the crystal is divided into overlapping spheres, each containing a spherical symmetrical potential for which the Kohn-Sham (KS) equation is solved directly. One-half of the spheres is centered around regular lattice sites, whereas the other half is centered around the highly symmetrical interstitial sites in order to fill the volume of the open diamond lattice. In our calculations, the positions of impurities forming a complex are restricted to the centers of these spheres only. If we place an impurity I on a lattice site, we shall denote it by I_{Si}, if we place it on a highly symmetrical interstitial site it will be indicated by I_i. Unfortunately, the use of the ASA does not allow to treat the effect of lattice relaxations around the impurity. The effect of this relaxation may be large, in particular, for the Li atom which is held in the interstitial position by undirected ionic forces.

From the self-consistent solution of Dyson's equation, we obtain the induced charge density, which is the difference between the charge density of the crystal with defects and the charge density of the unperturbed crystal. This density is composed of three contributions: The first one arises from the localized state solutions of the KS equations, denoted as single-particle gap states. The second contribution arises from resonancelike solutions of the KS equation in the valence bands of the host lattice. The contribution arising from the core states is generally small, except for the spin polarization (the core polarization), which is large for impurities with an open d shell, i.e., for the noble metal impurities.

III. RESULTS: TOTAL ENERGIES

We summarize the results of our LSDA calculations in terms of total energies, E^b_{tot}, and the binding energy, δE_{bind}, for the aggregate defects. In order to avoid the comparison of total energies for differently charged systems, we consider neutral systems: if the defect is positively (negatively) charged, we consider the charged defect plus the extra electron (hole) at the Fermi energy. For a defect in the charge state n, the total energy E_{tot} of the corresponding neutral system thus depends on the Fermi energy and is given by $E_{\mathrm{tot}} = E^b_{\mathrm{tot}} + nE_F$.

The binding energy, δE_{bind}, of an aggregate defect is defined as the difference between the sum of the total energies E_{tot} of the isolated point defects that form the aggregate defect and the total energy of the aggregate defect itself. As an example, we shall denote as $\delta E_{\mathrm{bind}}(\mathrm{Pt_{Si}} - \mathrm{Li}_i)^0_{\mathrm{orth}} = E_{\mathrm{tot}}(\mathrm{Pt}^-_{\mathrm{Si}}) + E_{\mathrm{tot}}(\mathrm{Li}_i)^+ - E_{\mathrm{tot}}(\mathrm{Pt_{Si}} - \mathrm{Li}_i)^0_{\mathrm{orth}}$ the energy gained by the formation of the aggregate defect from the constituents. Since $(\mathrm{Pt_{Si}} - \mathrm{Li}_i)^0_{\mathrm{orth}}$ can be considered to be formed combining $\mathrm{Pt}^0_{\mathrm{Si}}$ with Li^0_i or alternatively combining $\mathrm{Pt}^-_{\mathrm{Si}}$ with Li^+_i, we always use the charge state combination that leads to the lowest total energy.

A. Isolated point defects of the noble metals Au and Pt and of Li

Our results for the isolated substitutional Pt and Au point defects are similar to those obtained by Fazzio, Caldas, and Zunger[8] and by Beeler and Scheffler.[9] The electronic structure is described by the vacancy model proposed by Watkins,[10] as a vacancy interacting with the $5d$ states from the noble metal atom. Since the $5d$ states for Au and Pt are tightly bound, the corresponding single-particle states obtained from a solution of the KS equations form resonances in the valence band. This is schematically shown in Fig. 1(a) for isolated $\mathrm{Pt}^-_{\mathrm{Si}}$. These

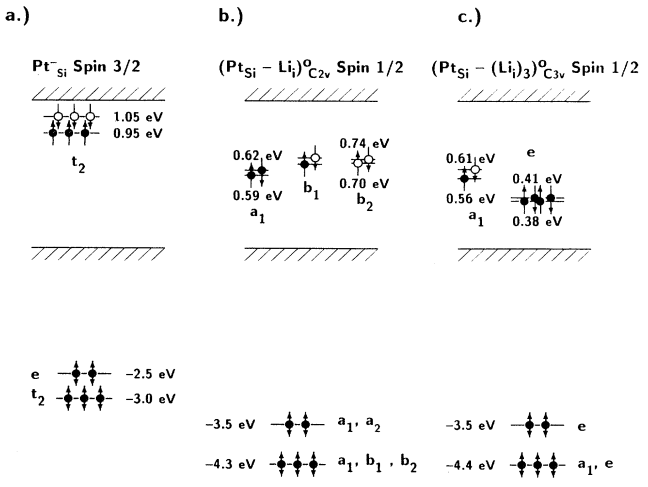

FIG. 1. (a) Defect-induced single-particle states for substitutional $\mathrm{Pt}^-_{\mathrm{Si}}$, (b) the orthorhombic $(\mathrm{Pt_{Si}} - \mathrm{Li}_i)^o_{C_{2v}}$ pair, and (c) the trigonal $[\mathrm{Pt_{Si}} - (\mathrm{Li}_i)_3]^o_{C_{3v}}$ aggregate defect A [see Fig. 6(a)], respectively. The energy scales for the gap states and for the valence band resonance states are different. The exchange splitting for the valence band resonance states is not shown. Full cicles represent occupied states (open circles represent empty ones).

resonances are essentially Pt $5d$ states with little admixture from the dangling vacancy bond states (the resonances are too broad to resolve the spin exchange splitting of these states). The antibonding states [called dangling bond hybrid (DBH) by Fazzio *et al.*[8]] are dangling bond states with some admixture from Pt p and d states. We find that about 6% of the total DBH charge density is p like in the Pt sphere and 11% is d like. The DBH single-particle states in Fig. 1(a) are split by the spin exchange interaction. Since in our calculations the orthorhombic lattice distortion is left out, we have a ground state with spin 3/2, in contrast to the experiment. While our results agree with those of Fazzio *et al.*,[8] there is disagreement with the structural model proposed by Ammerlaan and van Oosten,[11] which propose a d^9 electron configuration. Since the LSDA-DFT calculations are parameter free, there is no possibility of reconcileing our results with the model of Ref. 11. The results are also contrary to the famous Ludwig and Woodbury model[12] which, however, was developed for $3d$ transition metal impurities rather than for the $5d$ noble metals.

If the charge state of a defect is changed by adding an electron, the energies of all single-particle states change simultaneously. The electron removal energy $E^{(n)/(n-1)}$ of some point defect D is, therefore, not equal to the single-particle energy of the state that is occupied additionally. Instead it has to be determined as that position of E_F, where the total energies $E_{\rm tot}(D^{(n)})$ and $E_{\rm tot}(D^{(n-1)})$ for the two charge states are equal. For the isolated substitutional defects, we obtain $E^{+/0} = E_v +$ 0.52 eV (0.28 eV) and $E^{0/-} = E_v + 0.97$ eV (0.65 eV) for Pt_{Si} (Au_{Si}), which compare reasonably well with the experimental data[13] 0.32 eV (0.35 eV) and 0.94 eV (0.63 eV), respectively.

In Fig. 2, we compare the induced charge density of the isolated Pt^-_{Si} point defect with that of the isoelectronic Au^0_{Si}. The charge density arising from the d-like resonances is centered around the noble metal nucleus, while the more extended charge density arises predominantly from the occupied DBH. Since the nuclear charge of Au exceeds that of Pt by one elementary charge, the Au $5d$ resonance states are more localized and also lower in energy by about 2.5 eV. Therefore, the hybridization of the $5d$ electrons with the vacancy orbitals is less pronounced for Au_{Si} than for Pt_{Si} and the energetic position of the Au_{Si} DBH is lower than that of the Pt_{Si} DBH.

We find that the total energies for isolated interstitial Pt and Au point defects are higher than those for isolated substitutional Pt and Au point defects by about 3.2 eV for Pt and 4 eV for Au (see also Ref. 9). The localized states for the interstitial noble metals are very high in the gap and transform, according to the a_1 irreducible representation of the point group T_d. These states would, therefore, show a large contact hfi ($\sim$ 8 GHz for Pt_i) and no dipolar hfi, results that were not observed experimentally.

Li is known to be a superfast diffuser which has an extremely shallow donor level. In aggregate defects with noble metal atoms we expect, therefore, that Li_i will loose the outermost electron and predominantly act as a bare ion. For substitutional Li_{Si}, we find a vacancylike state in the gap, which transforms according to the t_2 irreducible representation of T_d. The total energy of Li_{Si}, with respect to Li_i^+, is higher by 4.5 eV for intrinsic Si. We, therefore, do not expect to have Li_{Si} present forming aggregate defects with noble metal defects. Furthermore, for Li_{Si} the $E^{0/-}$ level is at $E_v + 0.45$ eV. Since our samples are predominantly n type owing to the presence of Li_i, any substitutional Li could be negatively charged. This prevents the formation of aggregate defects with the noble metals Au and Pt, which are known for their electronegativity.

B. The orthorhombic ($Pt_{Si} - Li_i$) and ($Au_{Si} - Li_i$) pairs

Pt on a Si lattice site can form pairs with interstitial Li, which either exhibit trigonal symmetry (with Li_i being apart by a nearest neighbor distance from Pt_{Si}) or orthorhombic symmetry (in which case the Pt_{Si} and Li_i constituents are separated by a next nearest neighbor distance). For the orthorhombic pair, we show in Fig.

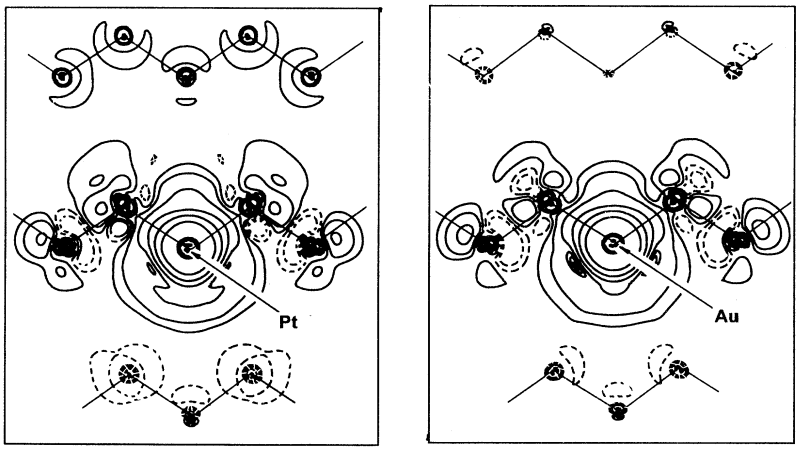

FIG. 2. Contour plot of the induced charge density of isolated Pt^-_{Si} (a) and Au^0_{Si} (b) in the (110) plane. Positive densities are indicated by full lines, negative densities by dashed lines, respectively. The nearest neighbor Si lattice points are connected by straight lines.

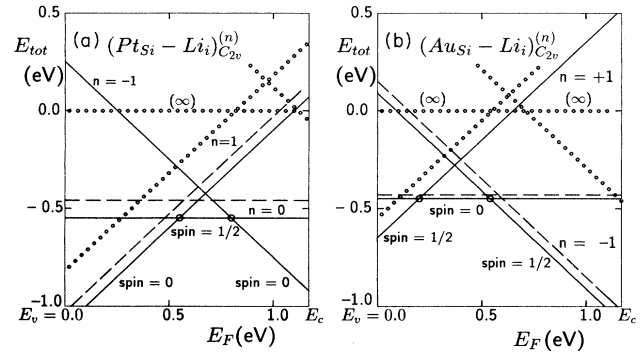

FIG. 3. Total energies for the orthorhombic $(Pt_{Si} - Li_i)^{(n)}$ pair (a) and the $(Au_{Si} - Li_i)^{(n)}$ pair (b) in the charge states n, as a function of the Fermi energy. Lines with positive slopes correspond to n =1, negative slopes belong to n = −1, and zero slopes indicate neutral pairs, respectively. Full lines correspond to the low-spin configurations (S = 0, and S = 1/2) and dashed lines correspond to the high-spin configurations (S = 2/2 and S = 3/2). The dotted lines correspond to the sum of the total energies of isolated Pt_{Si} and Li_i and circles mark ionization energies.

1(b) the single-particle energies. The main effect of the pair formation on the Pt^-_{Si} related electronic states is a shift of the 5d resonances by about 1 eV to lower energies, while the DBH states shift by about half this value. Of course, the lowering of the symmetry from T_d to C_{2v} splits the states that transform according to the t_2 and e irreducible representations of the T_d group into states that transform according to the a_1, b_1, and b_2 and to the a_1, and a_2 representations, respectively, of the C_{2v} point group, but these crystal field splittings are with 0.1 eV rather small. The exchange splitting between the spin-up and spin-down states is even smaller and, therefore, the ground states of the pairs are low-spin states for all charge states. This is shown in Fig. 3, where the total energies of the different charge and spin states of the $(Pt_{Si} - Li_i)_{C_{2v}}$ and $(Au_{Si} - Li_i)_{C_{2v}}$ pairs are compared with the sum of the total energies of the isolated point defects used to form the pairs. For both pairs in the neutral and negative charge state, we find $\delta E_{bind} \sim 0.5$ eV, while for the positive charge state the binding energy is smaller. Note that the neutral charge state of the $(Pt_{Si} - Li_i)_{C_{2v}}$ pair has the paramagnetic S = 1/2 ground state observed experimentally: For a homogeneous n-type crystal the negatively charged pair state will be diamagnetic in thermal equilibrium. For the orthorhombic $(Au_{Si} - Li_i)_{C_{2v}}$ pair, the ground state of the neutral charge state has zero spin, whereas both the positive and negative charge states have a S = 1/2 ground state.

The induced charge density of the $(Pt_{Si} - Li_i)_{C_{2v}}$ pair is shown in Fig. 4(a) as a contour plot in the (110) plane. The main difference to the corresponding Fig. 2 arises from the attractive potential of the Li ion, which increases the electron density in the interstitial region considerably. In contrast, the calculated total spin density, plotted in Fig. 4(b), is essentially the spin density of a singly occupied b_1 orbital and hardly affected by the presence of Li. From the spin density shown in Fig. 4(b), one can directly see that there are two equivalent Si nuclei for which the hfi is large, for the Si nuclei on the orthorhombic axis the spin density is extremely small. The spin density at the Li atom is practically zero.

The pair binding energies δE_{bind} of the $(Pt_{Si} - Li_i)_{C_{2v}}$ and $(Au_{Si} - Li_i)_{C_{2v}}$ pairs are shown as a function of the Fermi energy in Fig. 5. We also show corresponding data for trigonal $(Pt_{Si} - Li_i)_{C_{3v}}$ and $(Au_{Si} - Li_i)_{C_{3v}}$ pairs involving a single Li ion. Of course, the smallness of the energy differences of the binding energies for both configurations does not allow us to predict which of the configurations is more stable. In the samples studied experimentally in part I, no trace was found of these trigonal pairs.

C. The trigonal $[Pt_{Si}-(Li_i)_3]$ and $[Au_{Si}-(Li_i)_3]$ aggregate defects

The most intriguing feature of the trigonal aggregate defects is the prominent hfi with one Si nucleus, which was resolved by EPR. The fact that a single Si nucleus is

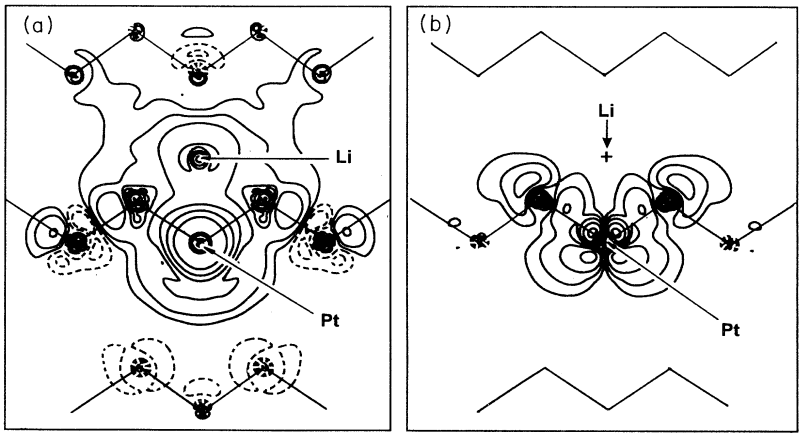

FIG. 4. Contour plot of the induced charge density (a) and of the total spin density (b) of the orthorhombic $(Pt_{Si} - Li_i)_{C_{2v}}$ pair in the (110) plane. Positive densities are indicated by full lines, negative densities by dashed lines, respectively.

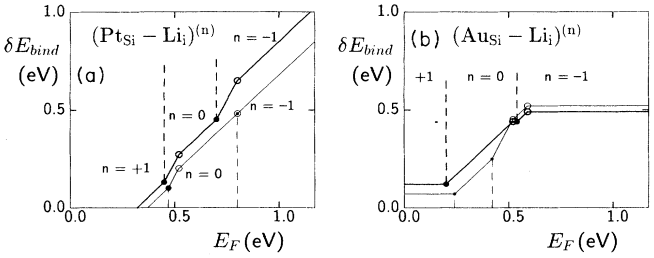

FIG. 5. Binding energies δE_{bind} for the orthorhombic (bold line) and the trigonal (light line) $(Pt_{Si} - Li_i)^{(n)}$ pairs (a) and $(Au_{Si} - Li_i)^{(n)}$ pairs (b), as a function of the Fermi energy. Full circles mark ionization energies for the pair while empty circles mark ionization energies of the isolated Pt_{Si} and Au_{Si}, respectively. The charge states of the pairs are denoted by n.

"highlighted" by a large spin density suggests that this nucleus is built in on a prominent lattice position. We have performed theoretical investigations of trigonal aggregate defects containing Si_i, which show that for aggregate defects involving Si_i, the calculated spin-density distribution is incompatible with the Si hfi observed experimentally.

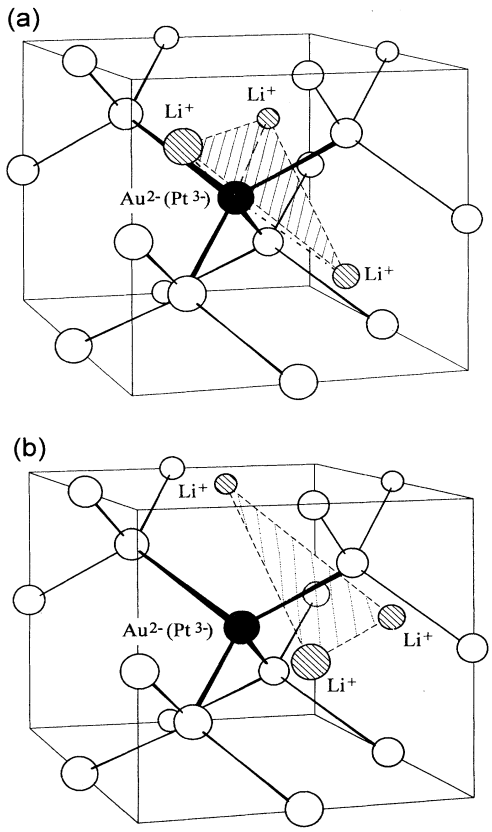

FIG. 6. Schematic representation of the atomic structures for the $[Pt_{Si} - (Li_i)_3]_{C_{3v}}$ aggregate defects A (a) and B (b).

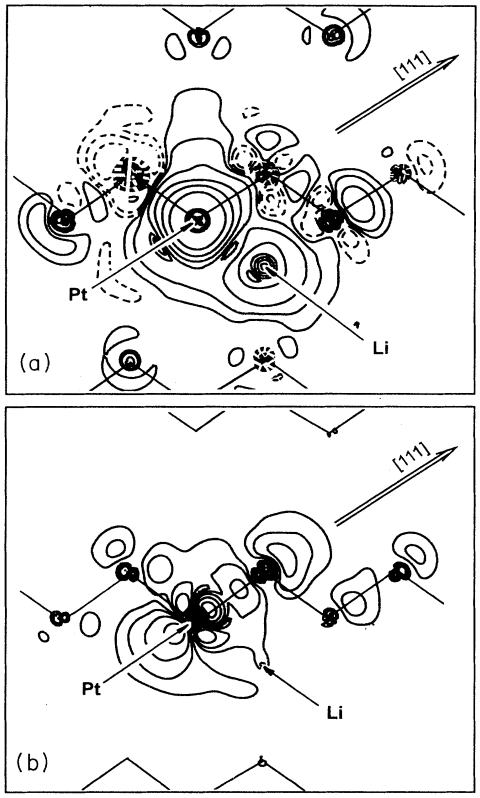

FIG. 7. Contour plot of the induced charge density (a) and of the total spin density (b) of the trigonal $[Pt_{Si} - (Li_i)_3]_{C_{3v}}$ aggregate in the (110) plane [defect A, see Fig. 6(a)]. Positive densities are indicated by full lines, negative densities by dashed lines, respectively. The trigonal axis is indicated by an arrow.

Since we know from ENDOR that three equivalent Li nuclei are present in the trigonal aggregate defects, the "highlighted" Si nucleus could be situated on a regular lattice position next to Pt_{Si} close to the three Li ions. We present results for two possible aggregate defects with trigonal symmetry, called aggregate defect A and aggregate defect B. These are sketched schematically in Fig. 6. In aggregate A the three Li atoms are separated by a nearest neighbor distance from the Pt in $\langle 111 \rangle$ directions, while for aggregate B the Li atoms are apart by a next nearest neighbor distance in $\langle 100 \rangle$ directions.

In the neutral charge state $[Pt_{Si} - (Li_i)_3]^0_{C_{3v}}$ of the platinum-related aggregate defect, the t_2-related single-particle DBH states are occupied by five electrons, which allows for a spin 1/2 state only. In its negative charge state, the aggregate defect is spinless as is the ground state of $[Pt_{Si} - (Li_i)_3]^+_{C_{3v}}$.

The presence of a trigonal crystal field splits the DBH into states transforming according to the a_1 and e irreducible representations of the group C_{3v}. In agreement with most trigonal pairs (see, e.g., the Fe-Al pair[14]), the single-particle state transforming according to a_1 is higher in energy than the e state. For the neutral aggregate defect $[Pt_{Si} - (Li_i)_3]^0_{C_{3v}}$, we thus find an orbital

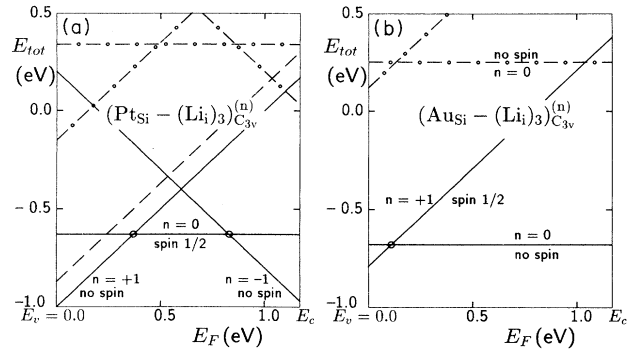

FIG. 8. Total energies for the trigonal $[Pt_{Si} - (Li_i)_3]^{(n)}_{C_{3v}}$ (a) and $[Au_{Si} - (Li_i)_3]^{(n)}_{C_{3v}}$ (b) aggregate defects A and B in the charge states (n), as a function of the Fermi energy. Lines with positive slope correspond to n =1, negative slopes belong to $n = -1$, and zero slopes indicate neutral pairs. Full lines correspond to the low-spin states ($S = 0$, and $S = 1/2$) and dashed lines correspond to the high-spin states ($S = 2/2$ and $S = 3/2$) of aggregate A. For aggregate B (dash-dotted lines) only the low-spin states are shown.

singlet as ground state. The single-electron states for aggregate A are shown in Fig. 1(c).

The induced charge density for the neutral aggregate defect A plotted in the (110) plane is shown in Fig. 7(a). It can be seen that the attractive potential of the three Li_i^+ ions leads to a considerable accumulation of electrons at the Pt and in the interstitial region occupied by the three Li ions. There is an accumulation of electron density near the Li nuclei, much more than one would expect for a shallow effective-mass-like state. The induced charge density at the Si ligand on the trigonal axis is practically zero and much smaller than that at the other Si ligands in the vicinity of the Pt atom. However, the spin density, Fig. 7(b), is centered around the [111] axis and clearly the Si nucleus on the trigonal axis will show a hfi that differs from the other Si ligands. In contrast to the charge density, the spin density at the Li nuclei is very small.

The total energies of the aggregate defects $[Pt_{Si} - (Li_i)_3]_{C_{3v}}$ and $[Au_{Si} - (Li_i)_3]_{C_{3v}}$ are shown in Fig. 8(a) and (b), respectively. For both aggregate defects, the configuration A is more tightly bound than configuration B by about 1 eV. We, therefore, conclude that the trigonal aggregates found experimentally are better described by configuration A. According to the results shown in Fig. 8 this charge state is present for p-type samples only. This result is in perfect agreement with the observation that for the gold-related trigonal defect the paramagnetic state is not observed, except during illumination. The binding energies δE_{bind} of the trigonal aggregate defects are rather large and vary strongly with the position of the Fermi level (Fig. 9). The large binding energy is compatible with the fact that these aggregate defects are formed at elevated annealing temperatures at the expense of the orthorhombic pairs.

D. Noble metal aggregate defects with two and four Li ions

Having observed the aggregate states of the noble metals Au and Pt with one Li ion and also with three Li ions, one might speculate that there are also aggregates with two and four Li ions. We, therefore, performed total energy calculations for an orthorhombic aggregate with two

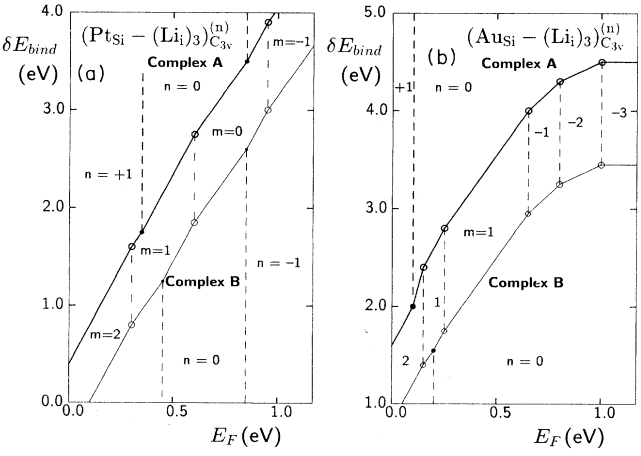

FIG. 9. Binding energies for the trigonal $[Pt_{Si} - (Li_i)_3]_{C_{3v}}$ aggregate defects A (full lines) and B (light lines), and for the trigonal $[Au_{Si} - (Li_i)_3]_{C_{3v}}$ complexes (b), as a function of the Fermi energy. Full circles mark ionization energies for the aggregates, while empty circles mark ionization energies of the isolated Pt_{Si} and Au_{Si}, respectively. The charge states of the aggregates are denoted by n, the charge state of the noble metal is denoted by m.

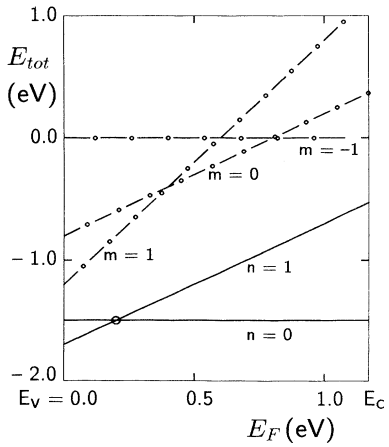

FIG. 10. Total energy for the tetrahedral $[Pt_{Si} - (Li_i)_4]^{(n)}$ aggregate defects in charge state n (full lines), compared with the sum of the total energies for the trigonal $[Pt_{Si} - (Li_i)_3]^{(m)}$ aggregate defects A and for one isolated Li_i^+ (dash-dotted lines).

Li ions. We find that the segregation reaction

$$2\,[\mathrm{Pt_{Si}} - (\mathrm{Li}_i)_2] \longrightarrow [\mathrm{Pt_{Si}} - (\mathrm{Li}_i)_3] + [\mathrm{Pt_{Si}} - (\mathrm{Li}_i)]$$

is exothermic by about 1.2 eV for all charge states of the aggregate and also for the aggregates with Au. It is, therefore, unlikely that $[\mathrm{Pt_{Si}} - (\mathrm{Li}_i)_2]$ or $[\mathrm{Au_{Si}} - (\mathrm{Li}_i)_2]$ aggregates are formed in larger concentrations.

According to our calculations, however, a tetrahedral $[\mathrm{Pt_{Si}} - (\mathrm{Li}_i)_4]_{T_d}$ aggregate defect should be quite stable. We present the total energy of this aggregate defect in Fig. 10 in comparison with the sum of the total energies of $[\mathrm{Pt_{Si}} - (\mathrm{Li}_i)_3]_{C_{3v}}$ and of an isolated Li_i^+ point defect. Obviously the tetrahedral aggregate defect should be quite stable in Li-rich material. Its observation will be hindered by the fact that it is paramagnetic in p-type material only. Since the state in the gap transforms according to the t_2 irreducible representation the tetrahedral aggregate defect could be subject to a Jahn-Teller (JT) distortion. This aggregate defect has not been observed to date as no p-type samples have been investigated so far.

According to our calculations, the analogous tetrahedral aggregate defect with Au should exists in the positive charge state only, $[\mathrm{Au_{Si}} - (\mathrm{Li}_i)_4]^+_{T_d}$. It should be tightly bound. Since there is no gap state it would be a perfect end product of a Au gettering process. However, it might be difficult to find such an aggregate experimentally.

IV. HYPERFINE INTERACTIONS

Our total energy calculations presented in the previous chapters strongly suggest that the orthorhombic defects observed experimentally (part I) are pairs of one Pt (Au) on a Si lattice site and one Li on the next nearest neighbor interstitial site, whereas the trigonal centers are aggregates of one Pt (Au) on a Si lattice site and three Li atoms on the nearest neighbor interstitial sites. We will show that these identifications are supported, if we extend our calculations to the g factors and hfi parameters.

For the noble metals Pt and Au, spin-orbit interaction cannot be neglected as has been demonstrated for isolated $\mathrm{Pt_{Si}}$ by Anderson *et al.*[3,4] We extend their treatment to our aggregate defects in this section. While our SCF calculations are based on charge densities in the limiting case of zero spin-orbit interaction taking full account of crystal fields, we switch to a description with LCAO single-particle wave functions. We include the spin-orbit interaction, using the single-particle wave functions of the SCF calculations as basis functions.

The eigenfunctions to the crystal fields and spin-orbit interaction depend basically on the ratio of the crystal field splitting parameters $\triangle_{\mathrm{cf}}$ to the effective spin-orbit splitting λ'. We take these ratios as free parameters, which are optimized to approximate the g factors and hfi with the noble metal nucleus. With the eigenfunctions thus determined, we calculate the hfi with the ^{7}Li nuclei and with the ^{29}Si ligand nuclei for both the orthorhombic and the trigonal complexes.

A. Orthorhombic pair defects

1. *Electronic structure*

Our SCF calculations show that for Pt-Li, and Au-Li, the t_2-derived DBH are vacancy orbitals ϕ_j^{vac} admixed with p-like and d-like Pt and Au orbitals, i.e., $\phi_j^{\mathrm{Pt}} = \cos\beta|d_j\rangle + \sin\beta|p_j\rangle$,

$$|t_{2,j}^{\mathrm{DBH}}\rangle = N\phi_j^{\mathrm{Pt}} + M\phi_j^{\mathrm{vac}}, \quad j = \xi,\eta,\zeta, \quad N^2 + M^2 = 1. \tag{2}$$

This t_2^{DBH} manifold is split under the influence of an orthorhombic field into states that transform like a_1, b_1, and b_2 in C_{2v}. Since for the noble metal d functions two different states transform according to the a_1 irreducible representation of the C_{2v} group,[3] we use the linear combination $|\phi_{a_1}^{\mathrm{Pt}}\rangle = \cos\gamma|d_{t_2}\rangle + \sin\gamma|d_e\rangle$. We make the approximation that the spin-orbit interaction in the t_2^{DBH} manifold comes entirely from those parts of the orbitals localized on the noble metal atom.[3,4] In the basis[15] $\{(b_1,\ ib_2,\ \bar{a}_1),\ (\bar{b}_1,\ -i\bar{b}_2,\ -a_1)\}$, the matrix of the total Hamiltonian — crystal field (tetragonal $\triangle_{D_{2d}}$, rhombic $\triangle_{\mathrm{rh}}$) plus spin-orbit interaction (λ) — separates into two identical blocks,

$$\begin{pmatrix} \triangle_{\mathrm{rh}} & -\frac{\lambda N^2}{2}\cos(2\beta) & -\frac{\lambda N^2}{2}q \\ -\frac{\lambda N^2}{2}\cos(2\beta) & -\triangle_{rh} & \frac{\lambda N^2}{2}z \\ -\frac{\lambda N^2}{2}q & \frac{\lambda N^2}{2}z & \triangle_{D_{2d}} \end{pmatrix}, \tag{3}$$

with $z = \cos^2\beta\,\mathsf{u}_1 - \sin^2\beta$, $q = \cos^2\beta\,\mathsf{u}_2 - \sin^2\beta$, $\mathsf{u}_1 = \cos\gamma + \sqrt{3}\sin\gamma$, and $\mathsf{u}_2 = \cos\gamma - \sqrt{3}\sin\gamma$. The crystal field splitting parameters $\triangle_{D_{2d}}$ and $\triangle_{\mathrm{rh}}$, which Anderson *et al.*[4] used to describe static JT distortions are now primarily due to the Li^+ ion. Diagonalization of (3) leads to three Kramers pairs $|+\rangle$ and $|-\rangle$ described by $\mathcal{S}' = \frac{1}{2}$ (with three sets of coefficients u, v, and w),

$$\begin{aligned} |+\rangle &= u|b_1\rangle - iv|b_2\rangle + w|\bar{a}_1\rangle, \\ |-\rangle &= u|\bar{b}_1\rangle + iv|\bar{b}_2\rangle - w|a_1\rangle. \end{aligned} \tag{4}$$

Each pair is split by the electronic Zeeman interaction,

$$H_Z = \mu_B(g_s\mathbf{S}\cdot\mathbf{B} + \mathbf{L}\cdot\mathbf{B}), \tag{5}$$

that leads[16] to the following g factors in terms of u, v, w, u_1, and u_2,

$$\begin{aligned} g_x &= g_s(1 - 2v^2 - 2w^2) + 4N^2vw[\cos^2\beta\,\mathsf{u}_1 - \sin^2\beta], \\ g_y &= g_s(1 - 2v^2) - 4N^2uw[\cos^2\beta\,\mathsf{u}_2 - \sin^2\beta], \\ g_z &= g_s(1 - 2w^2) + 4N^2uv\cos(2\beta). \end{aligned} \tag{6}$$

The indices x, y, and z refer to a defect symmetry-adapted coordinate system, which in terms of the crystal-adapted coordinate system (where x', y', and z' refer to the cubic axes) is given by $x \parallel [110]'$, $y \parallel [\bar{1}10]'$, and $z \parallel [001]'$.

2. *^{195}Pt and ^{197}Au hyperfine interaction*

(a) The hfi matrix elements. The Hamiltonian representing the hfi of an electron with a nuclear spin $\mathbf{I}$ has

TABLE I. SCF parameters used for the calculation of the hfi constants for ^{195}Pt and ^{197}Au. All values are in MHz.

Element	Defect	P_d	P_p	A_c
^{195}Pt	Pt-Li	1876	6000	−14.8
	Pt-Li$_3$	1875	6000	−9.6
^{197}Au	Au-Li	186	720	−3.4
	Au-Li$_3$	180	621	4.8

the general form

$$H_H = 2g_N\mu_B\mu_N \mathbf{I}\cdot\left(\frac{\mathbf{L}}{r^3}-\frac{\mathbf{S}}{r^3}+3\frac{\boldsymbol{r}(\mathbf{S}\cdot\boldsymbol{r})}{r^5}+\frac{8}{3}\pi\mathbf{S}\delta(\boldsymbol{r})\right). \tag{7a}$$

Here, g_N is the nuclear g factor of the nucleus with spin $\mathbf{I}$, and μ_N is the nuclear magneton. To this, we add the many-electron correction,

$$H_{\rm cp} = A_c(\mathbf{S}\cdot\mathbf{I}), \tag{7b}$$

where $A_c = 2g_N\mu_B\mu_N\frac{2}{3}\frac{4\pi}{2S}\sum_i\{|\varphi_i^+(0)|^2-|\varphi_i^-(0)|^2\}$ is a measure of the core polarization. The summation contains all core orbitals.[17] Using the formalism with an effective spin $\mathcal{S}'=\frac{1}{2}$, the matrix elements of (7) read in the principal axes system of the orthorhombic pair defect,

$$\mathcal{H}_H = A_{xx}\mathcal{S}_x\mathrm{I}_x + A_{yy}\mathcal{S}_y\mathrm{I}_y + A_{zz}\mathcal{S}_z\mathrm{I}_z, \tag{8}$$

where $\mathcal{S}_x$, $\mathcal{S}_y$, $\mathcal{S}_z$ denote effective spin operators (transforming according to the irreducible representations B_2, B_1, and A_2 of C_{2v}, respectively). In the case of hfi with ^{195}Pt or ^{197}Au, the corresponding eigenfunctions are (p-d)-like, thus the contact term in (7a) does not contribute while the core polarization (7b) leads to

$$\begin{aligned} A^c_{xx} &= (1-2v^2-2w^2)A_c,\\ A^c_{yy} &= (1-2v^2)A_c,\\ A^c_{zz} &= (1-2w^2)A_c. \end{aligned} \tag{9a}$$

The contributions of the first term in (7a) are obtained with the approximation[16] used for the evaluation of (5)

$$\begin{aligned} A^{\rm orb}_{xx} &= 4N^2vw[\cos^2\beta\mathsf{u}_1P_d-\sin^2\beta P_p],\\ A^{\rm orb}_{yy} &= -4N^2uw[\cos^2\beta\mathsf{u}_2P_d-\sin^2\beta P_p],\\ A^{\rm orb}_{zz} &= 4N^2uv[\cos^2\beta P_d-\sin^2\beta P_p], \end{aligned} \tag{9b}$$

with u_1, u_2 as in (6), and $P_d = 2g_N\mu_B\mu_N\langle r^{-3}\rangle_d$, $P_p = 2g_N\mu_B\mu_N\langle r^{-3}\rangle_p$. We denote the average values of r^{-3}, with respect to Pt or Au "valence" one-electron d and p orbitals by $\langle r^{-3}\rangle_d$ and $\langle r^{-3}\rangle_p$, respectively.

The final part of (7a)— the dipole-dipole interaction — leads to the following expressions:

$$\begin{aligned} A^{dd}_{xx} &= \frac{2}{7}[u^2-3uv+2v^2-w^2\mathsf{v}_1-uw\mathsf{v}_3]N^2P_d\cos^2\beta\\ &\quad+\frac{2}{5}[1+u^2+3uv-3uw]N^2P_p\sin^2\beta,\\ A^{dd}_{yy} &= -\frac{2}{7}[2u^2-3uv-v^2-w^2\mathsf{v}_2-vw\mathsf{v}_4]N^2P_d\cos^2\beta\\ &\quad-\frac{2}{5}[1+v^2+3uv-3vw]N^2P_p\sin^2\beta,\\ A^{dd}_{zz} &= \frac{2}{7}[1-w^2+w^2(\mathsf{v}_1+\mathsf{v}_2)+u\mathsf{v}_3+v\mathsf{v}_4]N^2P_d\cos^2\beta\\ &\quad-\frac{2}{5}[1+w^2-3(u+v)w]N^2P_p\sin^2\beta, \end{aligned} \tag{9c}$$

with $\mathsf{v}_1=\cos(2\gamma)-\sqrt{3}\sin(2\gamma)$, $\mathsf{v}_2=\cos(2\gamma)+\sqrt{3}\sin(2\gamma)$, $\mathsf{v}_3=3\cos(\gamma)+\sqrt{3}\sin(\gamma)$, and $\mathsf{v}_4=3\cos(\gamma)-\sqrt{3}\sin(\gamma)$.

(b) Comparison with EPR and ENDOR experiments. In order to find a reasonable set of parameters, we use the following procedure: The three eigenvalues of Eq. (3) and their corresponding eigenvectors are functions of the parameters $\delta_1=\frac{\triangle_{\rm rh}}{\lambda N^2}$, $\delta_2=\frac{\triangle_{D_{2d}}}{\lambda N^2}$, and β (neglecting γ in a first approximation). Since the three Kramers doublets have to be occupied with three electrons, we only have to consider the second eigenvalue with its corresponding eigenvector in a one-electron approximation. With its coefficients u, v, w, we calculate the g values (6) and the hyperfine constants (9). For the hfi parameters A_c, P_p, and P_d, we take the calculated SCF values listed in Table I (Ref. 18) and choose the parametes δ_1, δ_2, β, and N^2 to reproduce the experimentally determined data (in a second step we include γ). The results of this procedure are shown in Table II and Table III. Although we use a rather simple one-electron theory, the calculated total values are reasonably close to the measured values. Table III shows that for both pairs the orbital contributions to the g factors are relatively small compared to the contribution from the spin magnetism, but that the orbital contribution to the hfi constants can be comparable to the dipole-dipole contributions to the hfi constants. Thus, the hfi constants cannot be identified with spin densities even in a simple one-electron approximation. Since the experimental data are determined by EPR, we cannot compare the signs of our theoretical data to the experiment. The large deviations of the experimental g_y values from the free electron value g=2 is indicative of a larger admixture of noble metal t_2 orbitals into the DBH, as compared to the case of isolated platinum.[4] Therefore, our evaluation of the matrix elements including only those parts of the DBH that are localized on the noble metal becomes less accurate. We, therefore, consider the set of parameters given here as a first approximation in a perturbation series. A more appropriate evaluation of the matrix elements will retain the main features of our results: a ground state of nearly B_1 symmetry with an

TABLE II. Ground state parameters of the orthorhombic pairs as "seen" in EPR.

Element	u	v	w	N^2	β	γ	δ_1	δ_2
^{195}Pt	0.9698	−0.0631	−0.2356	0.22	0.1	0.0	4.8	6.6
^{197}Au	0.9527	−0.0138	−0.3036	0.123	0.0	−0.05	>40	>40

TABLE III. Calculated Zeeman and hfi (in MHz) parameters for ^{195}Pt and ^{197}Au of the orthorhombic pairs. $x \parallel [110]'$, $y \parallel [\bar{1}10]'$, $z \parallel [001]'$.

	Contrib.	g_x	g_y	g_z	A_{xx}	A_{yy}	A_{zz}
^{195}Pt	spin	1.762	1.984	1.777	−13.0	−14.7	−13.2
	orbital	0.012	0.198	−0.052	23.3	364.6	−96.0
	d-d				220.1	−235.6	39.7
	total	1.775	2.183	1.725	230.4	114.3	−69.5
	exp.	1.746	2.250	1.769	247.[a]	118.[a]	134.[a]
^{197}Au	spin	1.631	2.000	1.631	−2.8	−3.4	−2.8
	orbital	0.0	0.154	−0.003	0.2	28.7	−0.6
	d-d				10.8	−11.4	1.2
	total	1.631	2.154	1.728	8.2	13.9	−2.2
	exp.	1.548	2.456	1.629	<3[b]	8.5[a]	<3[b]

[a]EPR data, sign unknown.
[b]Unresolved but estimated from EPR linewidth.

admixture of A_1 symmetry, which is bigger than in the case of isolated platinum.[4]

3. ^{7}Li and ^{29}Si hyperfine interaction

The ^{7}Li and ^{29}Si hfi (Li-hfi, Si-hfi) are calculated in our LCAO scheme mixing symmetry-adapted linear combinations of ligand orbitals ($|s\rangle_A$, $|p_j\rangle_A$, with $A = \mathrm{Li}, \mathrm{Si}$, $j = x, y, z$) into the one-electron functions, which generate the electronic ground state. As we have found a ground state with nearly exact B_1 symmetry, we neglect all mixing of orbitals, due to spin-orbit interaction and deal with a pure b_1 orbital to calculate the Li-hfi and the Si-hfi.

For the calculation of the matrix elements of Eq. (7), where now **I** is the ligand nuclear spin, it is convenient to split the spin density into the part contained within the ligand atomic sphere, the spin density in the Pt sphere, and the rest (which is ignored). The first part can be evaluated directly as $A^{\mathrm{lig}}_{\mathrm{loc}} = \frac{4}{5} g^{\mathrm{lig}}_N \mu_B \mu_N \langle r^{-3} \rangle^{\mathrm{lig}}_p$, while the second part is given by $A^{\mathrm{lig}}_d = 2 g^{\mathrm{lig}}_N \mu_B \mu_N N^2 / R^3$ approximating the distribution of the magnetic moment in the Pt sphere by a point dipole.

(a) Lithium hyperfine interaction. Since the Li atom is located on a twofold rotation axis, we augment the b_1 orbital to

$$|b_1\rangle = \beta_0 |b_1\rangle_{\mathrm{vac}} + \beta_1 |p_x\rangle_{\mathrm{Li}}, \tag{10}$$

where $|b_1\rangle_{\mathrm{vac}}$ is the the eigenfunction of the orthorhombic crystal field constucted in Sec. IV A 1. From our SCF calculations, we know that Li s and p orbitals contribute with $\beta_1 \ll 1$.

Calculation of the matrix elements of (7) leads to

$$\begin{aligned} A^{\mathrm{Li}}_{xx} &= A^{\mathrm{Li}}_c + 2\beta_1^2 A^{\mathrm{Li}}_{\mathrm{loc}} - A^{\mathrm{Li}}_d, \\ A^{\mathrm{Li}}_{yy} &= A^{\mathrm{Li}}_c - \beta_1^2 A^{\mathrm{Li}}_{\mathrm{loc}} - A^{\mathrm{Li}}_d, \\ A^{\mathrm{Li}}_{zz} &= A^{\mathrm{Li}}_c - \beta_1^2 A^{\mathrm{Li}}_{\mathrm{loc}} + 2A^{\mathrm{Li}}_d. \end{aligned} \tag{11}$$

Using the results of our SCF calculations, we obtain hfi parameters, which have the same order of magnitude as the data determined experimentally (see part I). The smallness of the overall values prohibit quantitative comparison.

(b) Silicon hyperfine interaction. Since one large Si-hfi is measured experimentally, we restrict our analysis to this prominent Si-hfi and assign the values to Si$(1,1,1)'$. For shortness, we only explain the Si-hfi of Pt-Li and refer to the similarities for Au-Li.

According to Anderson *et al.*[4] the Si(111)′-hfi, with respect to the b_1 orbital, can be written as

$$(\mathcal{H}_{\mathrm{SH}})_{b_1} = \boldsymbol{\mathcal{S}} \cdot T_{(1,1,1)'} \cdot \mathbf{I}_{(1,1,1)'}, \tag{12}$$

where

$$T_{(1,1,1)'} = (M^2/2) T^0_{(1,1,1)'}. \tag{13}$$

$M^2/2$ describes the fraction of Si wave functions in the total wave function of the defect and

$$T^0_{(1,1,1)'} = \begin{pmatrix} a-b & 0 & 0 \\ 0 & a-b & 0 \\ 0 & 0 & a+2b \end{pmatrix}. \tag{14}$$

The Si hyperfine (hf) tensor is written in its principal axes system, where its z axis may be slightly tilted from $[111]'$ towards $[001]'$ [in the (110) plane]. The parameter a in Eq. (14) describes the contact interaction of the s part of the wave function of the Si atom, and b describes the dipole-dipole interaction. Neglecting core polarization, we have

$$\begin{aligned} a &= \frac{16\pi}{3} g^{\mathrm{Si}}_N \mu_B \mu_N |\phi_s(0)|^2 p_s, \\ b &= \frac{4}{5} g^{\mathrm{Si}}_N \mu_B \mu_N \langle r^{-3} \rangle_{\mathrm{Si}} p_p. \end{aligned} \tag{15}$$

Here, p_s and p_p denote the squared prefactors of the s and p part of the Si wave function. According to our SCF calculations, we find about 7.3% s and p fraction of the DBH localized on Si$(1,1,1)'$ with $(M^2/2)a = -60.8$ MHz and $(M^2/2)b = -7.1$ MHz. When we decompose

the measured values into the parameters a and b and approximately take $A_{[110]} = a + 2b$, we find reasonable agreement (−84 MHz, −4.8 MHz).

B. Trigonal defects

1. *Electronic structure*

The trigonal (Pt-Li_3) and (Au-Li_3) defects are treated using a modified vacancy model. Because of the close similarity of the (Pt-Li_3) and the (Au-Li_3), we restrict our discussion to the Pt related defect. We deal with linear combinations of Pt and vacancylike orbitals transforming according to the t_2 irreducible representation of T_d. The combined effect of spin-orbit interaction and a trigonal field caused by the three Li atoms and also by lattice relaxations leads to three new Kramers doublets, which have to be occupied with five electrons leaving one single unpaired electron. We approximate the many-electron ground state in a one-electron theory by this singly occupied level.

Our SCF calculations reveal an a_1 DBH as the highest one-electron level for both trigonal systems. The spin-orbit interaction mixes e orbitals into the a_1 orbitals leading to the $\mathcal{S}' = \frac{1}{2}$ eigenfunctions $|+\rangle$ and $|-\rangle$. For details, we refer to the Appendix. As in the case of the orthorhombic pair defects, it is useful to introduce a defect symmetry-adapted coordinate system. We choose $x \parallel [11\bar{2}]'$, $y \parallel [\bar{1}10]'$, and $z \parallel [111]'$, where the primed coordinates x', y', z' give the cubic axes of the crystal.

The calculation of the matrix elements of the Zeeman Hamiltonian (5) for the ground state functions (A3) of the trigonal complexes leads to the axially symmetric spin Hamiltonian,

$$\mathcal{H}_Z = \mu_B[g_\parallel \mathcal{S}_z \mathrm{B}_z + g_\perp(\mathcal{S}_x \mathrm{B}_x + \mathcal{S}_y \mathrm{B}_y)], \tag{16}$$

with

$$g_\parallel = g_s(g^2 - h^2) + 2g_{\tilde{l}}h^2,$$

$$g_\perp = g_s g^2 + \sqrt{8} g_{\tilde{l}} g h. \tag{17}$$

For $g_{\tilde{l}}$, g, and h, we refer to the Appendix.

2. *^{195}Pt and ^{197}Au hyperfine interaction*

(a) The hfi matrix elements. The ^{195}Pt hfi constants are calculated from the matrix elements of the hf Hamiltonian of Eq. (7) taken for the ground state (A3) and compared with the axially symmetric spin Hamiltonian,

$$\mathcal{H}_H = [A_\parallel \mathcal{S}_z \mathrm{I}_z + A_\perp(\mathcal{S}_x \mathrm{I}_x + \mathcal{S}_y \mathrm{I}_y)]. \tag{18}$$

The results are

$$\begin{aligned}
A_\parallel^c &= A_c(g^2 - h^2), \\
A_\perp^c &= A_c g^2, \\
A_\parallel^{\mathrm{orb}} &= g_{\tilde{l}} 2h^2(\cos^2\beta P_d - \sin^2\beta P_p), \\
A_\perp^{\mathrm{orb}} &= g_{\tilde{l}}\sqrt{8} g h(\cos^2\beta P_d - \sin^2\beta P_p), \\
A_\parallel^d &= \frac{2}{7}[1 + g^2 + \sqrt{2}gh]\cos^2\beta N^2 P_d \\
&\quad + \frac{2}{5}[1 + g^2 + 3\sqrt{3}gh]\sin^2\beta N^2 P_p, \\
A_\perp^d &= -\frac{2}{7}\left[1 + \frac{2gh}{\sqrt{8}}\right]\cos^2\beta N^2 P_d \\
&\quad - \frac{2}{5}[1 + 2h^2 - \sqrt{2}gh]\sin^2\beta N^2 P_p.
\end{aligned} \tag{19}$$

P_d and P_p are defined in Eq. (9b).

(b) Comparison with EPR and ENDOR. The procedure to calculate the EPR and ENDOR related parameters follows closely that for the orthorhombic pairs. We take A_c, P_d, and P_p (Table I)[18] from our SCF calculations and choose ϕ, β, and N^2 (A3) to approximate the Zeeman and noble metal hfi values. The results are given in Table IV. For Pt-Li_3, we show three different sets of ground state parameters and their corresponding Zeeman and hfi values. The values of $g_\perp$ are slightly too small when compared to the experimental data. The agreement could be improved at the expense of the agreement of the hf data. For Au-Li_3, we show only one set of ground state, Zeeman, and hfi data. The g values reveal the same deficit as the ones for Pt-Li_3. The hfi data are too small when compared to the experimental data but show correct signs.[19] The experimental data are determined by ENDOR and have equal signs (the experimental hfi data for ^{195}Pt of Pt-Li_3 are determined by EPR, thus only absolute values can be determined). However, despite their

TABLE IV. Three sets of ground state, Zeeman, and hfi (in MHz) parameters of (Pt-Li_3), and (Au-Li_3). $\parallel$ and $\perp$ refer to the trigonal axis.

	Fit	ϕ	g_l	β	$g_\perp$	$g_\parallel$	$A_\perp$	$A_\parallel$
	1	−0.1570	−0.40	0.40	2.0728	1.8884	−237	546
^{195}Pt	2	−0.1570	−0.40	0.45	2.0597	1.8900	−327	600
	3	−0.0627	−0.39	0.45	2.0351	1.9823	−339	694
	exp.				2.1654	1.8984	321.[a]	696.[a]
^{197}Au	1	−0.1885	−0.4	0.0	2.1380	1.8314	24.2	34.5
	exp.				2.2143	1.8517	36.3[b]	51.7[b]

[a]EPR data, sign unknown.

[b]Relative sign $A_\parallel$ to $A_\perp$ known from ENDOR.

TABLE V. Decomposition of Zeeman and hfi (in MHz) parameter of the third fit for the noble metal atoms of (Pt-Li_3) and (Au-Li_3).

	Contrib.	$g_\perp$	$g_\parallel$	$A_\perp$	$A_\parallel$
^{195}Pt	spin	1.9921	1.9842	−9.6	−9.5
	orbital	0.0429	−0.0020	26.6	−1.2
	d-d			−356.2	705.1
	total	2.0351	1.9823	−339.2	694.4
^{197}Au	spin	1.9297	1.8595	4.6	4.5
	orbital	0.2082	−0.0280	37.5	−5.1
	d-d			−17.9	35.1
	total	2.1380	1.8315	24.2	34.5

too small absolute values, our calculated data show the correct tendency (based on the positive sign of A_c).

A decomposition of our calculated data into the different contributions (Table V) reveals that the data for the hfi with ^{195}Pt of Pt-Li_3 is dominated by the dipole-dipole contributions, whereas the data for the hfi with ^{197}Au of Au-Li_3 results from a complex combination of spin and orbital momentum related parts. Bearing in mind that we deal with a one-electron theory in the sense of first order perturbation theory, we see a reasonable agreement of calculated and measured values.

3. *^{7}Li and ^{29}Si hyperfine interaction*

In this section, we try to explain the antisymmetry parameter of the Li-hfi and the Si-hfi again restricting our attention to the Pt related defect. We present the main ideas and results here and refer to the Appendix for details.

(a) Lithium hfi. As in the case of the orthorhombic pairs, we augment the one-electron orbitals of the defect by Li s and p functions, construct with these the eigenfunctions for an effective spin $\mathcal{S}' = \frac{1}{2}$, and calculate the matrix elements of the hf Hamiltonian (7) with respect to the electron operators, leaving the nuclear spin as an operator. Comparison of these matrix elements with the spin Hamiltonian

$$\mathcal{H}_{\text{Li-hfi}} = \mathcal{S} \cdot \boldsymbol{A} \cdot \mathbf{I}_{\text{Li}} \tag{20}$$

leads to the expressions for $\boldsymbol{A}_{ij}$ of Eq. (A6). With the approximation $h^2 \approx 0$ and $g^2 \approx 1$, the nonvanishing Fermi contact contributions of Eq. (A7) are

$$A^c_{xx} = A^c_{yy} = A^c_{zz} = \frac{1}{3}(\beta^a_1)^2\chi + A^{\text{Li}}_c,$$

$$A^c_{zx} = -A^c_{xz} = \frac{2}{3}gh\beta^a_1\beta^e_1\chi, \tag{21a}$$

with $\chi = \frac{16\pi}{3} g^{\text{Li}}_N \mu_B \mu_N |\phi^{\text{Li}}_s(0)|^2$ and A_c as in (7a). The nonvanishing a_1-restricted dipole-dipole parts of Eq. (A8) are

TABLE VI. Angular-momentum- and site-projected density of states of our SCF calculations as covalent admixture parameters (10^{-3}) for Li.

$(\beta^a_2)^2$	$(\beta^a_3)^2$	$\beta^a_3\beta^a_4$	$(\beta^a_4)^2$	$(\beta^e_2)^2$
5.444	0.059	−1.507	22.93	22.869

$$A_{xx} = \frac{5}{3}A^{\text{Li}}_d + \frac{1}{6}(\beta^2_3 - 2\sqrt{2}\beta_2\beta_3)A^{\text{Li}}_{\text{loc}},$$

$$A_{xz} = A_{zx} = \frac{2\sqrt{2}}{3}A^{\text{Li}}_d + \frac{1}{6}[\sqrt{2}(\beta^2_2 - \beta^2_3) - \beta_2\beta_3]A^{\text{Li}}_{\text{loc}},$$

$$A_{yy} = -A^{\text{Li}}_d - \frac{1}{6}(\beta^2_2 + \beta^2_3 + 2\sqrt{2}\beta_2\beta_3)A^{\text{Li}}_{\text{loc}}, \tag{21b}$$

$$A_{zz} = -\frac{2}{3}A^{\text{Li}}_d + \frac{1}{6}(\beta^2_2 + 2\sqrt{2}\beta_2\beta_3)A^{\text{Li}}_{\text{loc}},$$

where we omitted the superscript a for all coefficients β_i. The Fermi contact contribution contains an antisymmetrical part caused by spin-orbit interaction. Without core polarization, our SCF values (Tables I and VI) lead to an isotropic contact contribution of about 1.14 MHz, an antisymmetry parameter of $\triangle = 0.7$ MHz, and a dipole-dipole contribution of (in MHz)

$$A^{\text{Li}}_d = \begin{pmatrix} 1.79 & 0 & 0.58 \\ 0 & -1.16 & 0 \\ 0.58 & 0 & -0.63 \end{pmatrix}. \tag{22}$$

The eigenvalues of (22) can be parametrized[20] by $b = 0.96$ MHz and $b' = 0.20$ MHz in fair agreement with the measured values. According to our SCF calculations, we have $A_c = -0.89$ MHz. This leads to an isotropic total value of $a_{\text{tot}} = 0.25$ MHz, which is too small when compared to the measured value ($a_{\text{exp}} = 1.285$ MHz). Again, because of the relatively small absolute values and the complex competition between different many-electron effects (core and valence band polarization), we cannot expect perfect agreement of our calculated admixture coefficients: our calculated β_1 value is too small when compared to the experimental data. A larger β_1 value would also lead to a larger antisymmetry parameter, in general agreement with the experimental data.

The relatively small admixtures of e orbitals into the a_1 orbital, which turn out to be important for the antisymmetry just discussed, are unimportant for the calculation of the dipole-dipole contributions. Here, the major effect is caused by A^{Li}_d. We, therefore, calculate the parameters b and b' with full account of those many-electron effects, which are treated in our SCF calculations.[5–7,21] We obtain $b = 0.541$ MHz, $b' = 0.285$ MHz and the

eigendirection $[11\bar{2}] - 1.1°$.

(b) Silicon hfi. As a candidate for the observed large Si-hfi, we only have the $\mathrm{Si}(1,1,1)'$ neighbor to the Pt located on the trigonal axis. Augmenting the defect eigenfunctions by the $\mathrm{Si}(1,1,1)'$ orbitals, we calculate the hfi matrix elements and compare these with an axially symmetric spin Hamiltonian similar to that of Eq. (18). In the limit of nearly A_1 symmetry ($\phi = 0$), we obtain the following hfi parameters:[22]

$$A_{\perp}^{\mathrm{Si}(1,1,1)} = A_c^{\mathrm{Si}} + \gamma_2^2\chi^{\mathrm{Si}} - A_d^{\mathrm{Si}} - \gamma_3^2 A_{\mathrm{loc}}^{\mathrm{Si}},$$

$$A_{\parallel}^{\mathrm{Si}(1,1,1)} = A_c^{\mathrm{Si}} + \gamma_2^2\chi^{\mathrm{Si}} + 2A_d^{\mathrm{Si}} + 2\gamma_3^2 A_{\mathrm{loc}}^{\mathrm{Si}}. \tag{23}$$

Using our SCF results, we obtain $A_c^{\mathrm{Si}} + \gamma_2^2\chi^{\mathrm{Si}} \approx -50$ MHz, $A_d \approx -0.48$ MHz, and $\gamma_3^2 A_{\mathrm{loc}}^{\mathrm{Si}} \approx -17$ MHz. Comparing these values with their experimental counterparts ($|a| =$ 166 MHz and $|b| = 13$ MHz), we find our isotropic value by about a factor 3 too small, but the anisotropic value quite close to the measured value.

V. CONCLUSIONS

We have shown that our *ab initio* total energy calculations (treating many-electron effects in the LSDA to the DFT and disregarding lattice relaxations) combined with a subsequent inclusion of spin-orbit interaction effects provide a powerful tool for the microscopic defect identification. Our total energy calculations ruled out certain classes of defect models (containing interstitial noble metal atoms, substitutional Li, and Si self-interstitials) considering geometrical arrangements as well as electronic states, leaving the model of a pair defect consisting of a substitutional noble metal atom and a Li ion situated on an interstitial site at approximately next nearest neighbor distance along a cubic axis, for the measured orthorhombic aggregates and a defect model of a substitutional noble metal atom surrounded by three interstitial Li ions for the measured trigonal aggregates. On the basis of our total energy calculations, we explained why there are noble metal ion aggregates with one and three Li ions, respectively, but none with two Li ions, and predict the existance of a tetrahedral aggregate with four Li ions which, for Au as the noble metal, would have no state in the gap. However, with Pt it should be observable. We have shown that our calculated electronic structures of the isolated sustitutional noble metal atoms, as well as their related defect complexes studied experimentally (part I), can easily be interpreted in the vacancy model for impurities of $5d$ elements in Si first proposed by Watkins.[10]

In an extended vacancy model treating crystal fields and spin-orbit interaction in a one-electron approximation, we were able to calculate g factors and hfi constants for various nuclei (Au, Pt, Li, Si) that compare reasonably well with the measured values of part I.

ACKNOWLEDGMENT

Financial support from the Deutsche Forschungsgemeinschaft (DFG) is thankfully acknowledged.

APPENDIX A: VACANCY MODEL FOR TRIGONAL DEFECTS

1. Electronic structure

According to the vacancy model, we mix Pt p-like and d-like functions transforming according to the t_2 irreducible representation of T_d into the vacancy orbitals, see Eq. (2). The appropriate linear combinations of p and d functions are $|p_z\rangle$, $|p_x\rangle$, $|p_y\rangle$, and $|d_{3z^2-r^2}\rangle$, $-(\sqrt{\frac{2}{3}}|d_{x^2-y^2}\rangle + \sqrt{\frac{1}{3}}|d_{xz}\rangle)$, $\sqrt{\frac{2}{3}}|d_{xy}\rangle - \sqrt{\frac{1}{3}}|d_{yz}\rangle$. With these functions, we form eigenfunctions of a fictitious angular momentum:[23] $\tilde{l} = 1$

$$|\pm\tilde{1}\rangle = \mp\frac{|e_1\rangle \pm i|e_2\rangle}{\sqrt{2}}, |\tilde{0}\rangle = |a_1\rangle, \tag{A1}$$

with the effective orbital g factor of $g_{\tilde{l}} = -N^2\cos(2\beta)$.

According to the Wigner-Eckart theorem,[24] the trigonal splitting of the t_2 level and the spin-orbit interaction of the Pt $5d$ electrons can be written as

$$\mathcal{H}_{C_{3v}} = \delta_{\mathrm{trig}}\left(\tilde{l}_z^2 - \frac{2}{3}\right) + \lambda'\tilde{\boldsymbol{l}}\cdot\boldsymbol{S}, \tag{A2}$$

where we use $\lambda' = g_{\tilde{l}}\lambda$.

Occupation of the three eigenstates of $\mathcal{H}_{C_{3v}}$ with five electrons leaves the singly occupied Kramers pair described by $S' = \frac{1}{2}$,

$$|+\rangle = h|\tilde{1}\rangle\downarrow + g|\tilde{0}\rangle\uparrow,$$
$$|-\rangle = h|\widetilde{-1}\rangle\uparrow + g|\tilde{0}\rangle\downarrow, \tag{A3}$$

TABLE VII. Unnormalized symmetry-adapted linear combinations of Li s and p functions. The indices 2,3,4 number the Li positions $(1,1,-1)'$, $(-1,1,1)'$, $(1,-1,1)'$, respectively.

Γ	k	$\lvert\Gamma,k\rangle$
a_1	1	$\lvert s'\rangle_2 + \lvert s'\rangle_3 + \lvert s'\rangle_4$
	2	$\lvert p_{x'} + p_{y'}\rangle_2 + \lvert p_{y'} + p_{z'}\rangle_3 + \lvert p_{x'} + p_{z'}\rangle_4$
	3	$\lvert p_{z'}\rangle_2 + \lvert p_{x'}\rangle_3 + \lvert p_{y'}\rangle_4$
$e_{(1)}$	1	$2\lvert s'\rangle_2 - \lvert s'\rangle_3 - \lvert s'\rangle_4$
	2	$2\lvert p_{x'} + p_{y'}\rangle_2 - \lvert p_{y'} + p_{z'}\rangle_3 - \lvert p_{x'} + p_{z'}\rangle_4$
	3	$2\lvert p_{z'}\rangle_2 - \lvert p_{x'}\rangle_3 - \lvert p_{y'}\rangle_4$
$e_{(2)}$	1	$\lvert s'\rangle_3 - \lvert s'\rangle_4$
	2	$\lvert p_{y'} + p_{z'}\rangle_3 - \lvert p_{x'} + p_{z'}\rangle_4$
	3	$\lvert p_{x'}\rangle_3 - \lvert p_{y'}\rangle_4$

with $g = \cos\phi$ and $h = \sin\phi$, where ϕ is given by $\tan(2\phi) = \sqrt{2}\lambda'/(-\delta_{\rm trig} + \lambda'/2)$.

2. Lithium hyperfine interaction

Table VII shows the linear combinations of Li orbitals obtained by our SCF calculations. Because in ENDOR experiments only nuclear transitions of one nuclear spin are induced, we restrict ourselves to $\mathrm{Li}(1,1,-1)'$ functions and get the augmented orbitals,

$$|\Gamma\rangle = \beta_0^\Gamma |\Gamma\rangle_{\rm vac} + \sum_{k=1}^{3} \beta_k^\Gamma |\Gamma, k\rangle_2, \quad \Gamma \in \{a_1, e_{(1)}, e_{(2)}\}. \tag{A4}$$

Since $|e_{(2)}\rangle$ does not contain any $\mathrm{Li}(1,1,-1)'$ orbitals, the eigenfunctions of $\tilde{l}$ are real[25] and, therefore, we have orbital quenching.[26] Comparison of Eq. (7a) written as

$$H_H = \boldsymbol{N} \cdot \mathbf{I}_{\rm Li} \tag{A5}$$

with the spin Hamiltonian of Eq. (20) leads to[27]

$$A_{jx} + iA_{jy} = 2\langle -|N_j|+\rangle, \quad A_{jz} = 2\langle +|N_j|+\rangle, \tag{A6}$$

for $j = x, y, z$. We get the following nonvanishing Fermi contact and dipole-dipole interaction contributions:

$$\begin{aligned} A^c_{xx} &= A^c_{zz} = \frac{1}{3}[(g^2)(\beta_2^a)^2 - h^2(\beta_2^e)^2]\chi, \\ A^c_{yy} &= \frac{1}{3}[(g^2)(\beta_2^a)^2 + h^2(\beta_2^e)^2]\chi, \\ A^c_{zx} &= -A^c_{xz} = \frac{2}{3}gh\beta_2^a\beta_2^e\chi, \end{aligned} \tag{A7}$$

with χ defined in Eq. (21a), and[28]

$$\begin{aligned} A^d_{xx} &= \frac{5}{3}A_d^{\rm Li} + \frac{1}{6}\Big\{[g^2(\beta_4^a)^2 - h^2(\beta_4^e)^2] \\ &\quad -2\sqrt{2}(g^2\beta_3^a\beta_4^a - h^2\beta_3^e\beta_4^e)\Big\}A_{\rm loc}^{\rm Li} \\ &\quad +gh\frac{1}{3}\{\sqrt{2}(\beta_3^a\beta_3^e + \beta_4^a\beta_4^e) \\ &\quad +\tfrac{1}{2}(\beta_3^a\beta_4^e + \beta_4^a\beta_3^e)\}A_{\rm loc}^{\rm Li}, \\ A^d_{xz} &= \frac{2\sqrt{2}}{3}[g^2 - h^2]A_d^{\rm Li} + \frac{\sqrt{2}}{6}\Big\{g^2[(\beta_3^a)^2 - (\beta_4^a)^2] \\ &\quad -h^2[(\beta_3^e)^2 - (\beta_4^e)^2]\Big\}A_{\rm loc}^{\rm Li} \\ &\quad -\frac{1}{6}\left[g^2\beta_3^a\beta_4^a - h^2\beta_3^e\beta_4^e\right]A_{\rm loc}^{\rm Li} \\ &\quad +gh\frac{1}{3}\left[-\beta_3^a\beta_4^e + \sqrt{2}(\beta_3^a\beta_4^e + \beta_4^a\beta_3^e)\right]A_{\rm loc}^{\rm Li}, \\ A^d_{yy} &= -g^2A_d^{\rm Li} - \frac{1}{6}\Big\{g^2[(\beta_3^a)^2 + (\beta_4^a)^2] \\ &\quad +h^2[(\beta_3^e)^2 + (\beta_4^e)^2]\Big\}A_{\rm loc}^{\rm Li} \\ &\quad +\frac{\sqrt{2}}{3}\left[g^2\beta_3^a\beta_4^a + h^2\beta_3^e\beta_4^e\right]A_{\rm loc}^{\rm Li}, \\ A^d_{zx} &= A^d_{xz} + \frac{\sqrt{2}}{3}h^2A_d^{\rm Li} + gh\frac{1}{3}\left[\beta_4^a\beta_4^e + \beta_3^a\beta_3^e\right]A_{\rm loc}^{\rm Li}, \\ A^d_{zz} &= -\frac{2}{3}\left[g^2 - h^2\right]A_d^{\rm Li} + \frac{1}{6}\left[g^2(\beta_3^a)^2 - h^2(\beta_4^e)^2\right]A_{\rm loc}^{\rm Li} \\ &\quad +\frac{\sqrt{2}}{3}\left[g^2\beta_3^a\beta_4^a - h^2\beta_3^e\beta_4^e\right]A_{\rm loc}^{\rm Li} \\ &\quad +gh\frac{1}{3}\Big\{-\sqrt{2}(\beta_3^a\beta_3^e - \beta_4^a\beta_4^e) \\ &\quad +\frac{1}{2}(\beta_3^a\beta_4^e + \beta_4^a\beta_3^e)\Big\}A_{\rm loc}^{\rm Li}. \end{aligned} \tag{A8}$$

[1] P. Alteheld, S. Greulich–Weber, J.-M. Spaeth, H. Overhof, H. Weihrich, and M. Höhne, preceding paper, Phys. Rev. B **52**, 4998 (1995).
[2] H. H. Woodbury and G. W. Ludwig, Phys. Rev. **126**, 466 (1962).
[3] F. G. Anderson, J. Phys. Condens. Matter **3**, 4421 (1991); F. G. Anderson, C. Delerue, M. Lannoo, and G. Allan, Phys. Rev. B **44**, 10 925 (1991).
[4] F. G. Anderson, F. S. Ham, and G. D. Watkins, Phys. Rev. B **45**, 3287 (1992).
[5] U. v. Barth and L. Hedin, J. Phys. C **5**, 1629 (1972).
[6] R. O. Jones and O. Gunnarsson, Rev. Mod. Phys. **61**, 689 (1989).
[7] O. Gunnarsson, O. Jepsen, and O. K. Andersen, Phys. Rev. B **27**, 7144 (1983).
[8] A. Fazzio, M. J. Caldas, and A. Zunger, Phys. Rev. B **32**, 934 (1985).
[9] F. Beeler and M. Scheffler, Mater. Sci. Forum. **38-41**, 257 (1989).
[10] G. D. Watkins, Physica **117&118B**, 9 (1983).
[11] C. A. J. Ammerlaan and A. B. van Oosten, Phys. Scr. T **25**, 342 (1989).
[12] W. Ludwig, and H. H. Woodbury, Solid State Phys. **13**, 223 (1962).
[13] M. Schulz, in *Impurities and Defects in Group IV Elements and III-V Compounds,* edited by O. Madelung, Landolt-Börnstein, New Series, Group III, Vol. 22, Pt. B (Springer, Berlin, 1989), p. 207
[14] S. Greulich-Weber, A. Görger, J.-M. Spaeth, and H. Overhof, Appl. Phys. **A 53**, 147, (1991).
[15] We use the short-hand notation a_1 and $\bar{a}_1$ etc., for spin-up and spin-down one-particle orbitals.

[16] We evaluate the matrix elements of the orbital angular momentum only with the noble metal orbitals of the DBH.

[17] See, e.g., A. Abragam and B. Bleaney, *Electron Paramagnetic Resonance of Transition Ions* (Clarendon, Oxford, 1970), Chap. 17.6.

[18] The values of P_p and P_d listed in Table I are calculated from the angular-momentum-projected parts of the DBH within the atomic sphere of the noble metal atom and, therefore, differ from standard atomic data. The values of A_c in Table I result from two main parts: the polarization of the inner core electrons ("core polarization") and the polarization of the s states in the valence bands ("valence band polarization"). Both contributions differ in sign thus A_c is a small difference of rather large values.

[19] The theoretical hfi data could easily be improved (to nearly exactly the measured data) by using larger values of A_c ($\approx$ 21 MHz). Note that A_c results from a competition of core and valence band polarization and, therefore, is expected to be less accurate.

[20] J.-M. Spaeth, J. R. Niklas, and R. H. Bartram, *Structural Analysis of Point Defects in Solids*, edited by H.-J. Queisser (Springer, Berlin, 1992), p. 54.

[21] H. Overhof, H. Weihrich, and G. Corradi, Phys. Rev. B **45**, 9032 (1992), Eqs. (3), (4).

[22] Following our SCF results, we take into account Si s and p functions $|a_1\rangle = \gamma_1|a_1\rangle_{\text{vac}} + \gamma_2|s\rangle + \gamma_3|p_z\rangle$.

[23] *Electron Paramagnetic Resonance of Transition Ions* (Ref. 17), Chap. 14.2, p. 632ff.

[24] *Electron Paramagnetic Resonance of Transition Ions* (Ref. 17), Chaps. 13.5 and 19.4.

[25] Inside the Li(1,1,-1)′ atomic sphere. The total augmented defect orbitals form complex eigenfunctions of the effective angular momentum.

[26] We refer to the division of the spin density explained in subsection (IV A 3) and neglect all contributions to the matrix elements of $\frac{l_j}{r^3_{\text{Li}}}$ from outside the Li atomic sphere.

[27] *Electron Paramagnetic Resonance of Transition Ions* (Ref. 17), Chap. 17.4, Chap. 20.8.

[28] As in the case of the orthorhombic defects, we approximate for the dipole-dipole interaction $(\beta_0^a)^2 \approx (\beta_0^s)^2 \approx N^2$.